Robotica (2019) volume 37, pp. 560–574. © Cambridge University Press 2018
doi:10.1017/S0263574718001170

Stability and performance of haptic simulation involving interaction with non-passive virtual environment

Myeongjin Kim and Doo Yong Lee*

Department of Mechanical Engineering, Korea Advanced Institute of Science and Technology, 291 Daehak-ro, Yuseong-gu, Daejeon, 34141, Republic of Korea. E-mail: mj.k@kaist.ac.kr

(Accepted October 08, 2018. First published online: October 30, 2018)

SUMMARY

Previous researches on analysis of stability of haptic simulation largely assume that the virtual environment is passive. But the virtual environment can become non-passive due to various reasons including discretization errors and interaction dynamics between virtual tools and objects. This paper provides an analysis of the stability and performance of the haptic simulation involving non-passive virtual environment. The dynamic interaction between the virtual tools and the objects is modeled using the two-port networks. The analysis is carried out using a velocity and force mapping matrix for six-DOF simulation. New stability condition resulting from the analysis is applied to an example simulation of a one-DOF virtual wall. Maximum stiffness satisfying the stability condition established in the previous literature, and the proposed condition is compared with the maximum stiffness experimentally determined with various time steps. The newly proposed stability condition manifests less standard deviation of errors than the widely applied absolute stability condition.

KEYWORDS: Haptic interface, Haptic simulation, Virtual simulation, Absolute stability, Transparency

1. Introduction

Simulation providing both visual and haptic feedback is utilized in numerous applications including medical training.[1,2] The simulation should provide realistic visual and haptic interaction with the virtual environment while maintaining the stability of the simulation. Impedance transparency is frequently used to measure the performance of the simulation.[3,4] The stability is, however, often jeopardized by the discretization errors in the equations of the motion. It is also largely affected by the employed numerical-integration scheme, haptic rendering method, and contact-resolution method.[5–7]

Early studies focused on the interaction between rigid objects. Typical approaches render a coupling force instead of directly using the computed force[8] or apply an artificial damping force to the haptic device.[9–12] The artificial damping force sometimes causes the discontinuity in the feedback force, which decreases the realism of the simulation. Proxy and avatar represent the pose of the virtual tool and the haptic device, respectively, in the virtual coupling. The proxy connected using the virtual coupling[13] to the avatar follows the avatar by the coupling force. The proxy stays on the surface of a rigid object by the unilateral constraint[13,14] in contact motion. The proxy, rather than the avatar, is visually displayed for non-penetrating visuals. The maximum transmissible impedance can be restricted by the parameters of the virtual coupling for the absolute stability[6,15] or passivity[16] of the simulation. The pose of the proxy is determined by the unilateral constraint[13,14] for interaction with rigid objects. The coupling force is computed based on the distance between the proxy and the avatar. The benefit of the virtual coupling is that the stability problem can be decoupled from the virtual environment assuming it is passive.[8]

* Corresponding author. E-mail: leedy@kaist.ac.kr

https://doi.org/10.1017/S0263574718001170 Published online by Cambridge University Press

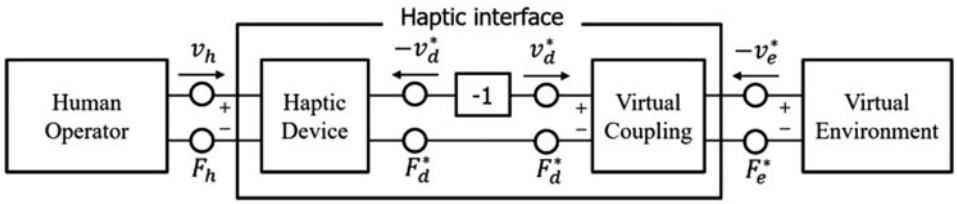


Fig. 1. A two-port network model of the haptic simulation composed of human, haptic device, virtual coupling, and virtual environment.[6]

The virtual coupling method is extended to interaction with deformable objects. Constraint-based contact force[17] or penalty force[18,19] are used to compute the contact force between the deformable object and proxy. The pose of the proxy is updated using the mass and rigid body dynamics of the proxy[7,17,20] because it is difficult to obtain constraints for the proxy to stay on the deformable surface. Simulation involving rigid body dynamics of the virtual tool and multi-point interaction between the virtual tool and deformable objects becomes non-passive.[7] The stability[6,15] and passivity conition[16] based on the assumption that the virtual environment are passive is no longer valid. Mass of the proxy must be small, and stiffness of the virtual coupling must be large for better impedance transparency. Some researchers tried to resolve the non-passive behavior in the virtual environment. Otaduy and Lin[7] proposed a linearized contact model to minimize the mass of the proxy while maximizing the stiffness of the virtual coupling. Discrete impulsive feedback force caused by discrete collision detection destabilizes the simulation. Xu and Barbič[21] tried to resolve the impulsive response in the case of multi-point contacts by employing adaptive scaling of the feedback force.

Previous researches proposed methods to increase the transparency of simulation. These methods, however, do not clearly and systematically explain how the discretized rigid body dynamics of the proxy, utilized numerical integration, and contact resolution affect the stability and transparency of the simulation. Even in the case that the virtual environment can be assumed passive, effects of the virtual environment should be considered in the analysis of the stability and transparency of the simulation to obtain more accurate and less conservative stability condition. This paper extends the two-port network analysis to account the virtual proxy, numerical integration, and contact resolution.

2. Stability and Transparency of Simulation

Let us consider simulation composed of a haptic device, a rigid virtual tool, virtual coupling, and deformable virtual objects. Adams and Hannaford[6] utilize the virtual coupling to resolve the active behavior of the haptic interface as shown in Fig. 1 such as impulsive force and oscillation caused by the discretized signal from the virtual environment. The parameters of the virtual coupling are determined by the two-port network analysis[6] assuming the human operator and the virtual environment are passive. Simulation which returns the feedback force depending on the velocity input is represented using the two-port network model as shown in Fig. 1.

F and v indicate the force and velocity, respectively. The subscripts h, d, and e denote the human, the haptic device, and the virtual environment, respectively. Discrete variables are indicated by asterisks. Velocity input of the human operator is sampled and fed to the virtual coupling via the haptic device. Coupling force is computed based on the velocity of the human and the virtual environment. The coupling force is then conveyed to the human and virtual environment. The virtual environment is updated by the coupling force. The negative sign in the velocity is used to maintain consistency with the network theory formalism. The relation between the human and the virtual environment is represented in the frequency domain by a hybrid matrix which is a matrix of the transfer functions as in (1).

$$\begin{bmatrix} F_h \\ -v_e^* \end{bmatrix} = \begin{bmatrix} h_{11} & h_{12} \\ h_{21} & h_{22} \end{bmatrix} \begin{bmatrix} v_h \\ F_e^* \end{bmatrix}. \tag{1}$$

Stability and performance are determined by the absolute stability[22] and the impedance transparency,[23] respectively. If the simulation satisfies (2) introduced in ref. [6], then the system between the human and the virtual environment is unconditionally stable assuming the human and the virtual environment

https://doi.org/10.1017/S0263574718001170 Published online by Cambridge University Press

are passive.

$$\begin{aligned} &\mathrm{Re}\,(h_{11}) \geq 0, \quad \mathrm{Re}\,(h_{22}) \geq 0, \\ &\eta\,(\omega) = -\cos\,(\angle h_{12}h_{21}) + \frac{2\mathrm{Re}\,(h_{11})\,\mathrm{Re}\,(h_{22})}{|h_{12}h_{21}|} \geq 1, \quad \forall\,\omega \geq 0, \\ &\text{where,} \quad \cos\,(\angle h_{12}h_{21}) = \frac{\mathrm{Re}\,(h_{12}h_{21})}{|h_{12}h_{21}|}. \end{aligned} \tag{2}$$

$\eta(\omega)$ is called the network stability parameter. The impedance transparency of the simulation means an accurate rendering of the impedance of the virtual object, Z_e to the human hand. The transmitted impedance, Z_{to}, is represented by (3).

$$Z_{\mathrm{to}} = \frac{h_{11} + \Delta h\, Z_e}{1 + h_{22}Z_e}, \text{ where } \Delta h = h_{11}h_{22} - h_{12}h_{21}. \tag{3}$$

Perfect transparency is achieved when the transmitted impedance, Z_{to}, is equal to the environment impedance, Z_e. If the input of the human manipulation is scaled by the position scaling factor, α_x and the force feedback is scaled by the force scaling factor, α_f for the macro-micro system,[24] then the perfect transparency is represented as shown in (4).

$$Z_{\mathrm{to}} = \frac{\alpha_f}{\alpha_x} Z_e. \tag{4}$$

It is usually reasonable to assume the human as a passive operator.[13] The virtual environment, however, often becomes non-passive. The motion of the proxy can generate additional kinetic energy due to errors in the numerical integration. Contact force between the proxy and the deformable objects can have discontinuity due to varying number of contact points. The discontinuity of the contact force causes oscillation of the haptic device. The non-passive behavior of the motion of proxy and contact force can be resolved by implicit integration and previous methods.[21,25]

Even when the virtual environment is passive, integration errors can supply excessive energy or absorb more energy beyond the governing law of physics. The specific numerical integration utilized, virtual coupling, and contact resolution method must be considered in the analysis of the stability and the transparency for more accurate and less conservative condition.

2.1. Haptic device

The basic assumptions[6] for the haptic device are followed. Dynamics of the haptic device is modeled in the continuous-time domain. Zero-order holder (ZOH) is approximated by a low-pass filter with a steady-state gain of and 90° phase lag at the Nyquist frequency. Update rate of the virtual environment is considered by the time step, dT in the ZOH. Feedback force is conveyed using the ZOH to the continuous-time domain. The hybrid matrix of a one-DOF haptic device is previously derived as shown in (5). Z_d and ZOH are the discretized impedance of the haptic device (6) and the normalized ZOH (7), respectively.

$$\begin{bmatrix} F_h \\ -v_d^* \end{bmatrix} = \begin{bmatrix} Z_d\,(z) & \alpha_f \cdot \mathrm{ZOH}\,(z) \\ -1 & 0 \end{bmatrix} \begin{bmatrix} v_h \\ F_d^* \end{bmatrix}, \tag{5}$$

$$Z_d\,(z) = m_d \frac{2}{\Delta T} \frac{z-1}{z+1} + b, \tag{6}$$

$$\mathrm{ZOH}\,(z) = \frac{1}{2} \frac{z+1}{z}. \tag{7}$$

The time step, ΔT is constant and an inverse of the update rate of the simulation. The m, b, and α_f denote the mass, damping coefficient of the haptic device, and the force scaling factor, respectively.

https://doi.org/10.1017/S0263574718001170 Published online by Cambridge University Press

Table I. Relations among discrete force, velocity, and position according to the numerical integration.

Integration scheme	Difference equation	$V(z)/F(z)$	$X(z)/V(z)$
Explicit	$x_{k+1} = x_k + v_k \Delta T$ $v_{k+1} = v_k + F_k/m \cdot \Delta T$	$\frac{1}{z-1}\frac{\Delta T}{m}$	$\frac{\Delta T}{z-1}$
Implicit	$x_{k+1} = x_k + v_{k+1} \Delta T$ $v_{k+1} = v_k + F_{k+1}/m \cdot \Delta T$	$\frac{z}{z-1}\frac{\Delta T}{m}$	$\frac{z\Delta T}{z-1}$
Semi-implicit	$x_{k+1} = x_k + v_{k+1} \Delta T$ $v_{k+1} = v_k + F_k/m \cdot \Delta T$	$\frac{1}{z-1}\frac{\Delta T}{m}$	$\frac{z\Delta T}{z-1}$
Midpoint (same with velocity-verlet)	$x_{k+1} = x_k + v_{k+1/2} \Delta T$ $v_{k+1/2} = v_k + F_k/2m \cdot \Delta T$ $v_{k+1} = v_{k+1/2} + F_{k+1}/2m \cdot \Delta T$	$\frac{z+1}{z-1}\frac{\Delta T}{2m}$	$\frac{2z\Delta T}{(z-1)(z+1)}$
Newmark (same with HHT)	$x_{k+1} = x_k + v_k \Delta T + F_\gamma/2m \cdot \Delta T^2$ $v_{k+1} = v_k + F_\gamma/m \cdot \Delta T$ $F_\gamma = (1-\gamma)F_k + \gamma F_{k+1}$	$\frac{\gamma z - \gamma + 1}{z-1}\frac{\Delta T}{m}$	$\frac{z+1}{z-1}\frac{\Delta T}{2}$

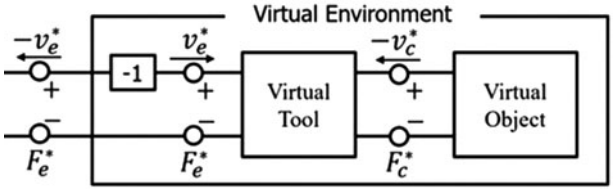


Fig. 2. Subnetwork for the virtual environment.

2.2. Numerical integration

Numerical integration is included in the hybrid matrix to account the discretization effect of the simulation. The velocity and position of the virtual tool are determined by the difference equation of the numerical-integration scheme. The relation between the discrete force, velocity, and position can be obtained using Z-transform of the difference equation in the frequency domain. Time step of the simulation is accounted by $z = e^{s\Delta T}$. The resulting relations for the representative numerical-integration schemes such as explicit, implicit, semi-implicit, midpoint, velocity-verlet, Newmark, and HHT are shown in Table I.

The subscript k indicates the simulation step of the variables. The m and F_k is the mass and the force applied to the virtual tool, respectively. Forces applied to the tool are the contact force between the tool and the object and the coupling force between the tool and the user manipulation. Different forces can also be applied to the tool depending on the simulation design. The following analysis uses the semi-implicit integration as an example because of its simplicity and relatively more stable performance. The following analysis also can be straightforwardly applied for other integration schemes.

2.3. Virtual coupling

The virtual environment is further elaborated into the virtual tool wielded by the haptic device through the virtual coupling, and the virtual objects as shown in Fig. 2. The subscript c denotes variables of contact between the virtual tool and the virtual object.

Figure 3 shows the free body diagram of the virtual environment. The virtual coupling connecting the haptic device and the virtual tool is shown in Fig. 3. The k_{vc} and c_{vc} are the spring and damping coefficient of the virtual coupling, respectively. Displacement of the haptic device generates a coupling force in the virtual coupling. The force is exerted to the mass center of the virtual tool, and moves the virtual tool. Force is generated between the virtual tool and the virtual object when they contact. The pose of the virtual tool is determined by the coupling force, contact force, and dynamics of the virtual tool.

https://doi.org/10.1017/S0263574718001170 Published online by Cambridge University Press

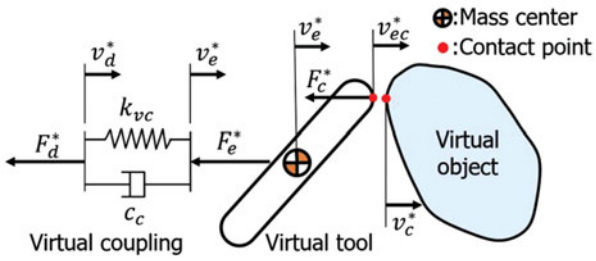


Fig. 3. Free body diagram of the virtual coupling and contact between the virtual tool and virtual object.

Force according to the difference in the position and velocity between the haptic device and the virtual tool is conveyed to the haptic device and the virtual tool in the opposite directions.

$$F_d^* = k_{vc}\left(\alpha_v x_d^* - x_e^*\right) + c_{vc}\left(\alpha_v v_d^* - v_e^*\right). \tag{8}$$

α_v denotes the position (velocity) scaling factor. The position of the haptic device is represented using the first differential approximation as $x_d^* = \Delta T \cdot z/(z-1) \cdot v_d^*$ in the Z-domain. The velocity and position are updated using numerical integration in the virtual environment. The position of the virtual tool can be obtained as $x_e^* = \Delta T \cdot z/(z-1) \cdot v_e^*$ from Table I. The impedance of the virtual coupling, which represents the relation between the difference in velocity and the coupling force, is obtained in the Z-domain as given in (9)

$$Z_{vc}(z) = c_{vc} + \frac{k_{vc} \cdot \Delta T \cdot z}{z-1}. \tag{9}$$

The hybrid matrix of the virtual coupling can be acquired as in (10) following the previously established approach.

$$\begin{bmatrix} F_d^* \\ -v_e^* \end{bmatrix} = \begin{bmatrix} 0 & -1 \\ -\alpha_v & -\dfrac{1}{Z_{vc}(z)} \end{bmatrix} \begin{bmatrix} v_d^* \\ F_e^* \end{bmatrix}. \tag{10}$$

The difference in the virtual coupling used in this paper from the previous works is the sign of the force exerted to the virtual environment. The reason for this difference is that the virtual coupling formulated in this paper elaborates in detail transmission of the force from the haptic device to the virtual environment.

2.4. Virtual interaction

Interaction in the virtual environment is processed in three steps in general. The virtual tool is moved according to its rigid-body dynamics and exerted forces. Collisions between the virtual tool and virtual objects are detected next. Contact force is then computed using the employed interaction model such as the penalty[26] or constraint-based method.[17] The contact force is conveyed to the mass center of the virtual tool and the virtual objects. This paper defines the impedance of the virtual tool to represent the relationship between the exerted force on the center of the virtual tool and the velocity of the virtual tool. The impedance of the virtual tool, in the case of semi-implicit integration, is obtained as shown in (11) using the Z-transform from Table I.

$$Z_t(z) = \frac{m_e}{\Delta T}(z-1) + c_e. \tag{11}$$

m_e, c_e, and ΔT indicate the mass, damping, and time step of the virtual environment, respectively. The contact force between the virtual tool and the virtual object depends on the applied interaction model. A single contact point is considered in this paper. The contact force is usually computed based on the penetration depth and velocity. The penetration depth can be represented by velocity using Table I according to the applied integration scheme.

https://doi.org/10.1017/S0263574718001170 Published online by Cambridge University Press

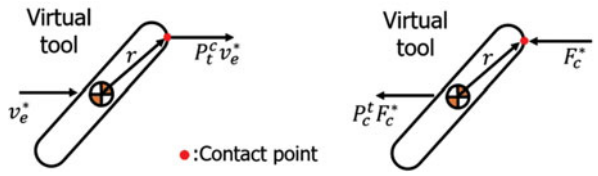


Fig. 4. Velocity and force mapping in the virtual tool.

This paper defines the impedance of contact, Z_c, which represents the relationship between the contact force and penetration velocity at the contact point. The penetration velocity is represented as the velocity difference at the contact point. The contact occurs at the surface of the virtual tool and the object. The velocity of the contact point, v_{ec}^*, on the tool is the same as the velocity of the mass center, v_e^*, in the case of one-DOF. A mapping matrix is required to represent the velocity of the contact point with the velocity of the mass center for six-DOF. The details of the velocity mapping matrix are explained next. It is difficult to specify the velocity of the virtual object at the contact point using the velocity of the mass center in case of deformable objects because the surface of the deformable model is not fixed. The velocity of the virtual object v_c is specified as the velocity at the contact point. The contact force can be represented as the contact impedance and penetration velocity as given in (12).

$$F_c^* = Z_c(v_{ec}^* - v_c^*). \tag{12}$$

It is possible to analyze the stability of the simulation in this way without considering the deformable objects when the virtual objects are passive. The maximum admissible contact impedance obtained in the proposed analysis can be used to restrict the maximum contact force regardless of the contact-resolution method employed for the stability of the simulation. The equivalent force and torque are conveyed in case of six-DOF. A hybrid matrix of the interaction in the virtual environment can be acquired as given in (13) using (11) and (12).

$$\begin{bmatrix} F_e^* \\ -v_c^* \end{bmatrix} = \begin{bmatrix} -Z_t(z) & -1 \\ -1 & \dfrac{1}{Z_c(z)} \end{bmatrix} \begin{bmatrix} v_e^* \\ F_c^* \end{bmatrix}. \tag{13}$$

2.5. Six-DOF simulation

The hybrid formulation can be extended to six-DOF haptic simulation. The impedance used in the formulation can be independently defined for each translational and rotational direction. The impedance matrices can be defined in a diagonal matrix. The velocities and forces of the haptic device and the virtual environment are represented using a 6×1 vector composed of three translational and three rotational components. The velocity and force of the virtual tool and virtual object at the contact point are represented using a translational 3×1 vector. A velocity and force mapping matrix is required to extend the result to the six-DOF haptic simulation.

The velocity of the contact point is a translational velocity determined by the geometry of the virtual tool, the translational (v_1, v_2, v_3), and angular $(\omega_1, \omega_2, \omega_3)$ velocity of the mass center. A velocity vector of the contact point is equal to the summation of the translational velocity vector of the mass center and the cross product of the angular velocity vector and the point vector, $r(r_1, r_2, r_3)$, as shown in Fig. 4.

A skew symmetric of the position vector is applied to represent the cross product as a matrix-vector product. The velocity of the tool at the contact point can be defined by the product of the velocity of the mass center and the velocity mapping matrix P_t^c determined by the geometry of the virtual tool as in (14) using the skew symmetric.

$$v_{ec}^* = P_t^c v_e^* = \begin{bmatrix} 1 & 0 & 0 & 0 & -r_3 & r_2 \\ 0 & 1 & 0 & r_3 & 0 & -r_1 \\ 0 & 0 & 1 & -r_2 & r_1 & 0 \end{bmatrix} \begin{bmatrix} v_1 \\ v_2 \\ v_3 \\ \omega_1 \\ \omega_2 \\ \omega_3 \end{bmatrix}. \tag{14}$$

https://doi.org/10.1017/S0263574718001170 Published online by Cambridge University Press

A force exerted to the contact point makes equivalent translational and rotational forces to the mass center. The equivalent translational force is the same as the force exerted to a contact point. The equivalent torque is represented as a cross product of a position vector, r and a contact force vector, $F_c(f_1, f_2, f_3)$. The equivalent force and torque F_e^* can be defined by multiplication of the contact force vector of the mass center and the force mapping matrix P_t^c determined by the geometry of the virtual tool using (15).

$$F_e^* = P_c^t \cdot F_c^* = \begin{bmatrix} 1 & 0 & 0 \\ 0 & 1 & 0 \\ 0 & 0 & 1 \\ 0 & -r_3 & r_2 \\ r_3 & 0 & -r_1 \\ -r_2 & r_1 & 0 \end{bmatrix} \cdot \begin{bmatrix} f_1 \\ f_2 \\ f_3 \end{bmatrix}. \tag{15}$$

A hybrid matrix of the six-DOF haptic simulation which represents the velocity and force relationship between the human and the contact point of the virtual object is derived by combining the above relationships as delineated in (16).

$$\begin{bmatrix} F_h \\ -v_c^* \end{bmatrix} = \begin{bmatrix} Z_d + \alpha_f \mathrm{ZOH}\left(\frac{Z_{vc}}{Z_{vc}+Z_t}\right)\alpha_v Z_t & \alpha_f \mathrm{ZOH}\left(\frac{Z_{vc}}{Z_{vc}+Z_t}\right) P_c^t \\ -\alpha_v P_t^c + \frac{P_t^c}{Z_{vc}}\left(\frac{Z_{vc}}{Z_{vc}+Z_t}\right)\alpha_v Z_t & \frac{I}{Z_c} + \frac{P_t^c}{Z_{vc}}\left(\frac{Z_{vc}}{Z_{vc}+Z_t}\right) P_c^t \end{bmatrix} \begin{bmatrix} v_h \\ F_c^* \end{bmatrix}. \tag{16}$$

The stability condition of the six-DOF simulation including the discretization effect of the rigid body dynamics of the virtual tool, virtual coupling, and contact impedance is acquired as shown in (17)–(19) by applying (2). The mapping parameter depends on the contact point on the virtual tool and the shape of the virtual tool. All the possible mapping parameters can be examined before the simulation because the shape of the rigid virtual tool is predetermined before the simulation. The mapping parameter generating the maximum force or torque is required to obtain the maximum admissible impedances.

$$\mathrm{Re}\left(Z_d + \alpha_f \mathrm{ZOH}\left(\frac{Z_{vc}}{Z_{vc}+Z_t}\right)\alpha_v Z_t\right) \geq 0, \forall\, \omega \geq 0, \tag{17}$$

$$\mathrm{Re}\left(\frac{I}{Z_c} + \frac{P_t^c}{Z_{vc}}\left(\frac{Z_{vc}}{Z_{vc}+Z_t}\right) P_c^t\right) \geq 0, \ \forall\, \omega \geq 0, \tag{18}$$

$$\begin{aligned} \eta(\omega) = &-\cos\left(\alpha_f \mathrm{ZOH}\left(\frac{Z_{vc}}{Z_{vc}+Z_t}\right) P_c^t \alpha_v P_t^c \left(\frac{I}{Z_{vc}}\left(\frac{Z_{vc}}{Z_{vc}+Z_t}\right)\alpha_v Z_t - I\right)\right) \\ &+2\mathrm{Re}\left(Z_d + \alpha_f \mathrm{ZOH}\left(\frac{Z_{vc}}{Z_{vc}+Z_t}\right)\alpha_v Z_t\right) \mathrm{Re}\left(\frac{I}{Z_c} + \frac{P_t^c}{Z_{vc}}\left(\frac{Z_{vc}}{Z_{vc}+Z_t}\right) P_c^t\right) \geq 1, \ \forall\, \omega \geq 0. \end{aligned} \tag{19}$$

The impedances in (17) have positive values except for the virtual tool. The impedance of the virtual tool can be negative according to the employed integration scheme. The semi-implicit integration shows, for example, negative because $z = e^{s\Delta T}$ is smaller than one. The impedance of the haptic device must be larger than the second term of the real part. Physical meaning of this is that the haptic device must absorb the energy from the non-passive virtual environment for stability. Condition (18) is satisfied because the impedances of the contact and the virtual coupling are positive. Smaller impedances of contact and the virtual coupling increase the stability margin in (18). Physical meaning of this is that less stiff contact and coupling force is desirable for stable simulation. System parameters are related to the network stability parameter, $\eta(\omega)$. The relation between the network stability parameter (19) and the system parameters is numerically analyzed in Section 3.

https://doi.org/10.1017/S0263574718001170 Published online by Cambridge University Press

Table II. Parameters of the numerical simulation.

Symbol	Quantity	value
m_d	Mass of the haptic device[5]	0.022 kg
b	Damping of the haptic device[5]	0.01 Ns/m
m_e	Mass of the virtual tool	0.1 kg
c_{vc}	Damping of the virtual coupling	1.0 Ns/m
k_{vc}	Stiffness of the virtual coupling	100 N/m
m_{vo}	Mass of the virtual object	1 kg
c_{vo}	Damping of the virtual object	0.06 Ns/m
k_{vo}	Stiffness of the virtual object	300 N/m
dT	Time step	0.002 s

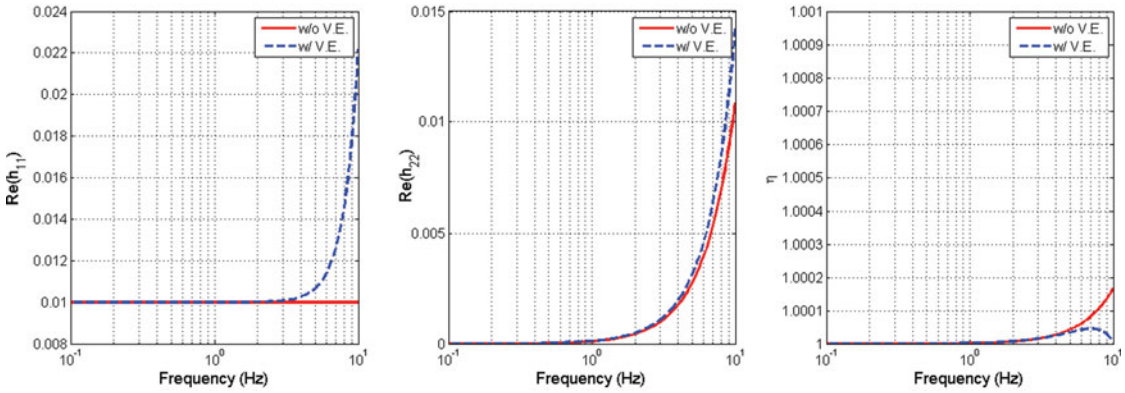


Fig. 5. Effect of the stiffness of the virtual coupling to the previous[6] and the proposed absolute stability conditions involving the virtual environment (V.E.) (Left: Re(h_{11}), Middle: Re(h_{22}), Right: $\eta(\omega)$).

The h_{11} and h_{22} have to be zero, and h_{12} and $-h_{21}$ has to be the force and position scaling factors for perfect transparency, respectively.[3,24] The impedance of the haptic device and the virtual tool should be equal to zeros to make h_{11} equal to zero. Physical meaning of this is that the inertia and damping of the haptic device and virtual tool must be zero for perfect transparency. The impedance of contact and virtual coupling should be large to make h_{22} equal to zero. This means that stiff virtual coupling and contact stiffness is required. ZOH($Z_{vc}/(Z_{vc}+Z_t)$) should be one to make h_{12} equal to one. And $(Z_t/(Z_{vc}+Z_t))$ must be zero to make $-h_{21}$ equal to one. The impedance of the virtual coupling must be much larger than the impedance of the virtual tool. And the ZOH should be one to make both h_{12} and $-h_{21}$ equal to one.

The impedance of the haptic device and virtual tool should be small for transparency but large for stability. The impedance of the virtual coupling and contact should be small for stability but large for transparency. This indicates that stiff virtual coupling and contact force increases the transparency of the simulation but can cause a stability problem during the simulation.

3. Numerical Analysis

A one-DOF numerical simulation is analyzed using the proposed hybrid matrix to see the effect of the system parameters on the stability and the transparency of the simulation. The simulation is composed of a haptic device, a virtual tool, and a rigid object connected to a fixed wall by a spring and damper. The semi-implicit integration and the penalty-based contact resolution are employed. Parameters of the numerical simulation are set as shown in Table II.

The absolute stability condition[6] is compared with the proposed condition. Figure 5 shows the effect of the stiffness of the virtual coupling on the previous and the proposed stability conditions. The proposed stability condition is less conservative than the previous stability condition on Re(h_{11}) and Re(h_{22}) because the proposed stability condition includes the inertia of the virtual tool.

https://doi.org/10.1017/S0263574718001170 Published online by Cambridge University Press

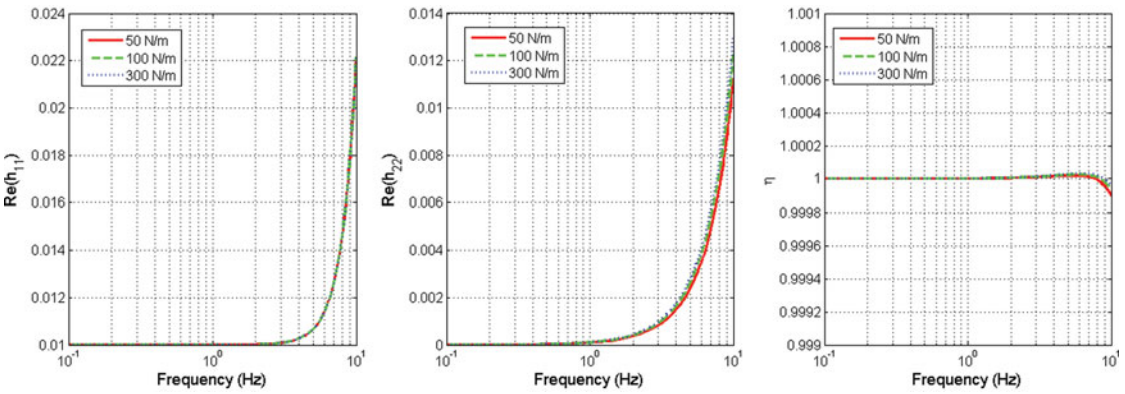


Fig. 6. Effect of the stiffness of the contact impedance to the proposed absolute stability conditions (Left: Re(h_{11}), Middle: Re(h_{22}), Right: $\eta(\omega)$).

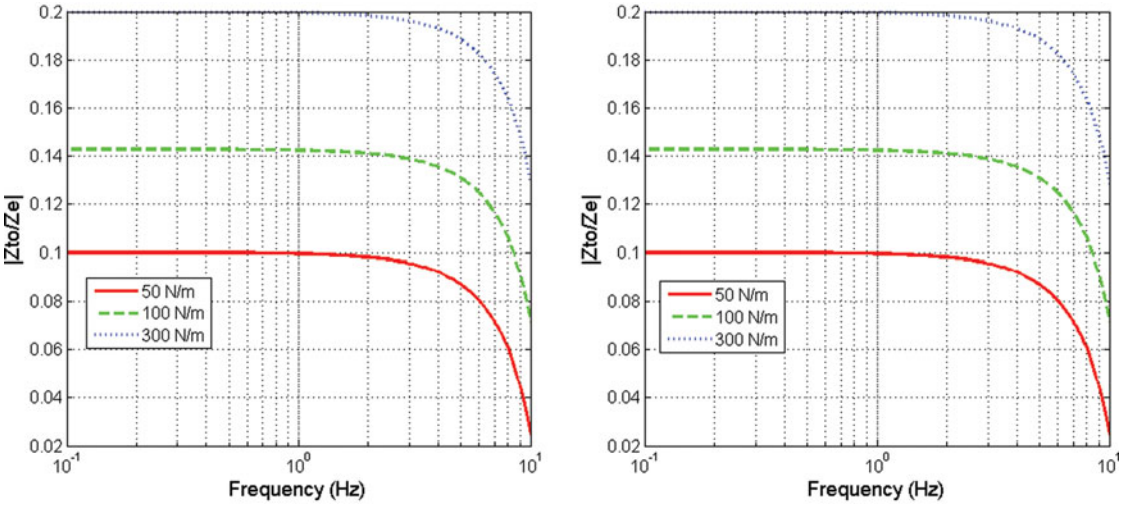


Fig. 7. Effect of the stiffness of the virtual coupling (Left) and the contact impedance (Right) to the ratio of the transmitted impedance to the environment impedance.

Figure 6 shows the effect of the stiffness of the contact impedance on the stability that cannot be analyzed using the previous stability condition. The effect of the contact stiffness is negligible compared to the effect of the stiffness of the virtual coupling.

Effect of the virtual coupling and the contact impedance to the impedance transparency is measured using the ratio of the transmitted impedance (3) to the impedance of the virtual object as shown in Fig. 7. The ratio is one in the ideal case. The maximum transparency in the simulation is 0.2. The reason for the low transparency is that the stiffness of the virtual coupling and contact impedance set to low and the mass of the virtual tool set to large for the stability. The effect of the contact impedance on the transparency is the same as the virtual coupling. This means that higher stiffness of the contact impedance increases the transparency with less loss of the stability than the higher stiffness of the virtual coupling.

Figure 8 shows the effect of the tool mass on the stability. Larger mass increases the stability margin on Re(h_{11}) and Re(h_{22}) but causes stability problem on $\eta(\omega)$. This means that higher mass enhances the stability margin of the haptic device and virtual environment but causes stability problem on the interaction between the haptic device and the virtual environment. Physical meaning of this is that the inertia of the virtual mass enhances the stability robustness on the haptic device and the virtual tool, but the kinetic energy stored in the virtual mass may cause instability during the interaction.

The minimum, $|Z_{\text{tomin}}|$ and the dynamic range, $|Z_{\text{towidth}}|$ of the transmitted impedance[4] is analyzed to see the effect of the virtual tool mass on the transparency. Figure 9 shows $|Z_{\text{tomin}}|$ and $|Z_{\text{towidth}}|$ according to the virtual tool mass. $|Z_{\text{tomin}}|$ has to be zero when the transmitted impedance during the

https://doi.org/10.1017/S0263574718001170 Published online by Cambridge University Press

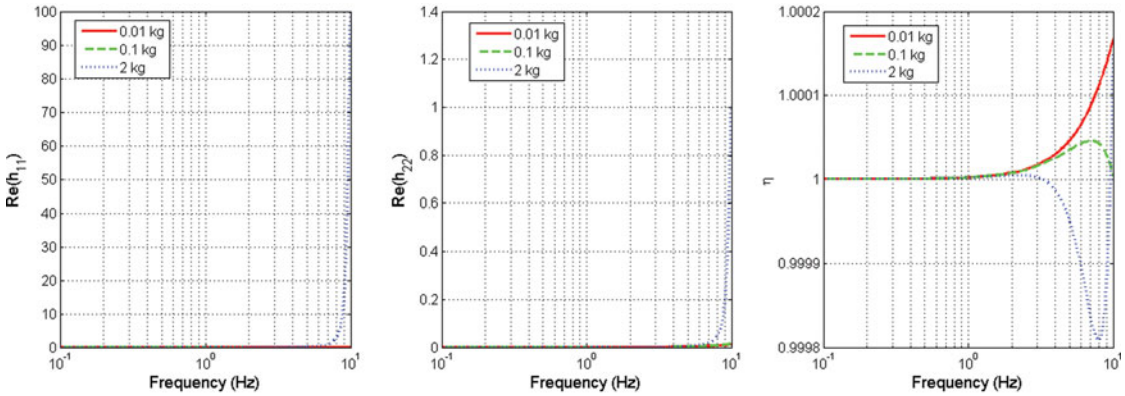


Fig. 8. Effect of the mass of virtual tool to the proposed absolute stability conditions (Left: Re(h_{11}), Middle: Re(h_{22}), Right: $\eta(\omega)$).

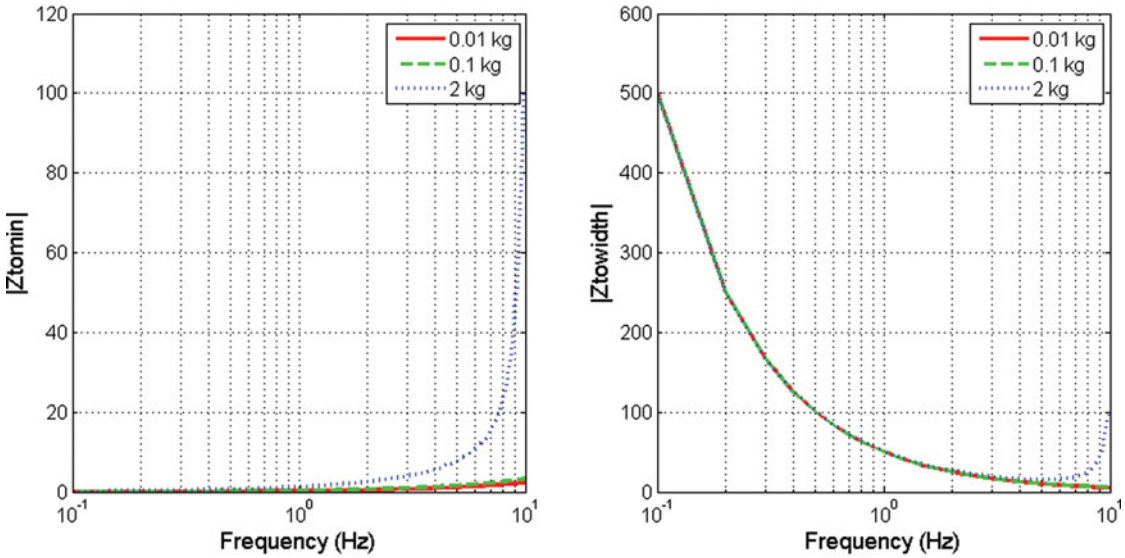


Fig. 9. Effect of the mass of the virtual tool to $|Z_{\text{tomin}}|$ (Left) and $|Z_{\text{towidth}}|$ (Right).

free motion is equal to zero. The minimum transmitted impedance increases as the tool mass increases. It means that the human operator feels the inertia force of the tool mass during the free motion. The inertia force exponentially increases as the manipulation velocity increases. Figure 9 shows that $|Z_{\text{towidth}}|$ is affected by the manipulation velocity, but not by the tool mass. $|Z_{\text{towidth}}|$ decreases as the manipulation velocity increases.

Effect of the employed numerical-integration scheme to the stability and transparency of the simulation is analyzed for the semi-implicit, implicit, midpoint, and Newmark. Figure 10 shows the stability conditions of the numerical integrations. The implicit scheme shows the highest stability robustness. The implicit integration is better than the midpoint and Newmark integration for the interactive simulation because the implicit, midpoint, and Newmark have similar computational complexity. The stability robustness of the semi-implicit is smaller than other integration schemes. But the computational load is smaller than other integrations.

Figure 11 shows that the effect of the integration scheme to $|Z_{\text{tomin}}|$ and $|Z_{\text{towidth}}|$. The integration scheme does not affect the transparency. It is well known that the small time step increases the stability of the interactive simulation. Figure 12 shows the effect of the time step of the virtual environment to $|Z_{\text{tomin}}|$ and $|Z_{\text{towidth}}|$. The results show that the time step does not affect the transparency of the simulation.

https://doi.org/10.1017/S0263574718001170 Published online by Cambridge University Press

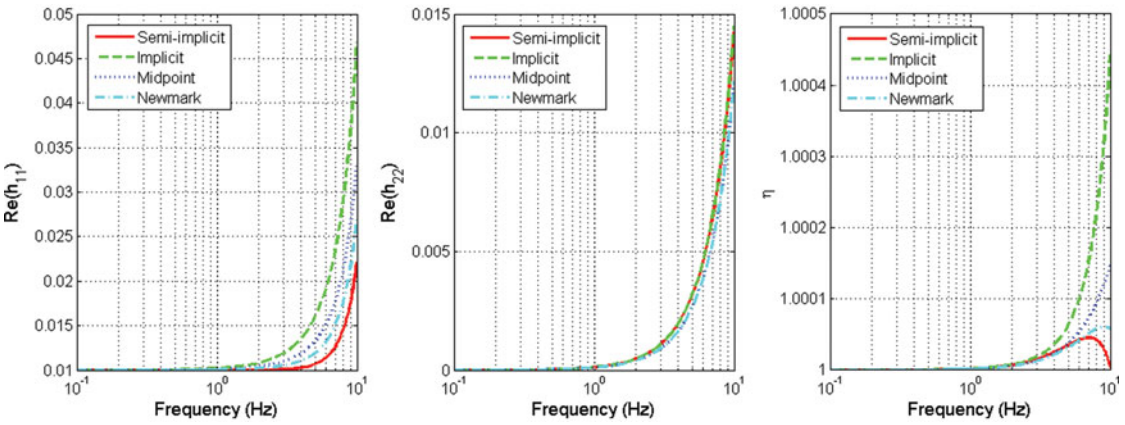


Fig. 10. Effect of the numerical-integration scheme to the proposed stability condition (Left: Re(h_{11}), Middle: Re(h_{22}), Right: $\eta(\omega)$).

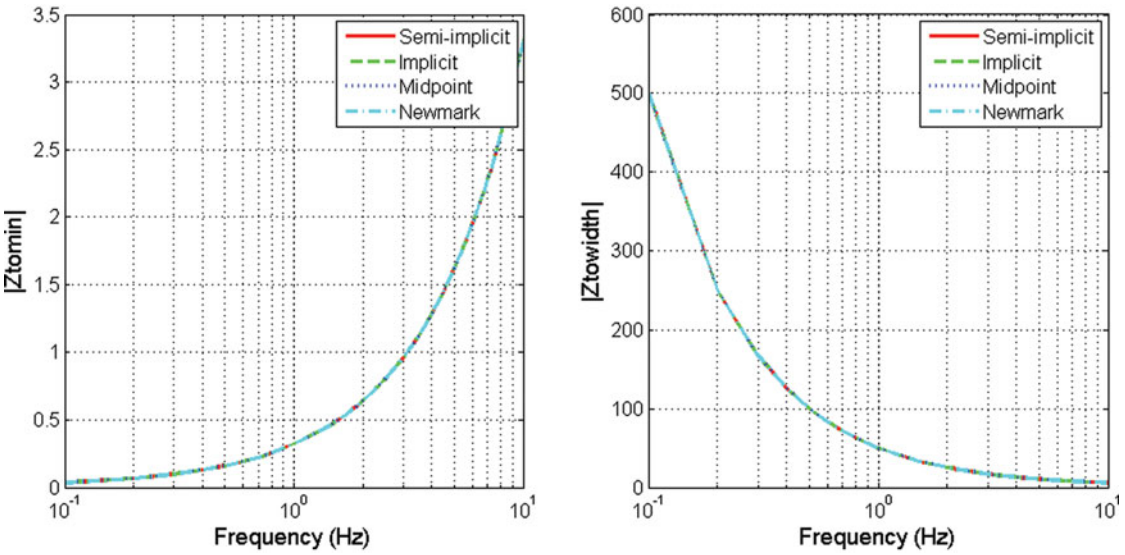


Fig. 11. Effect of the numerical-integration scheme to $|Z_{\text{tomin}}|$ (Left) and $|Z_{\text{towidth}}|$ (Right).

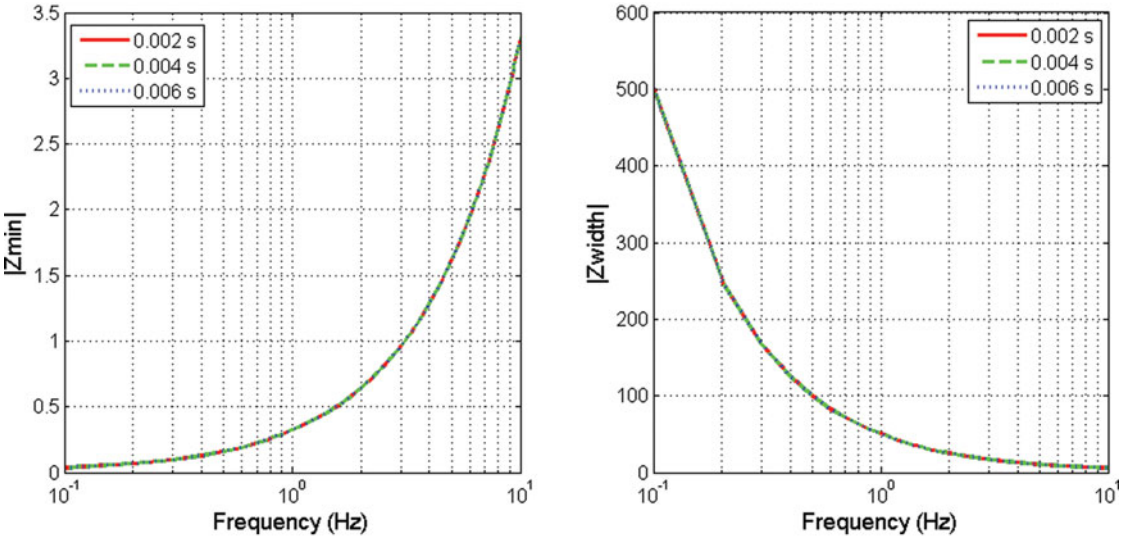


Fig. 12. Effect of the time step to $|Z_{\text{tomin}}|$ (Left) and $|Z_{\text{towidth}}|$ (Right).

https://doi.org/10.1017/S0263574718001170 Published online by Cambridge University Press

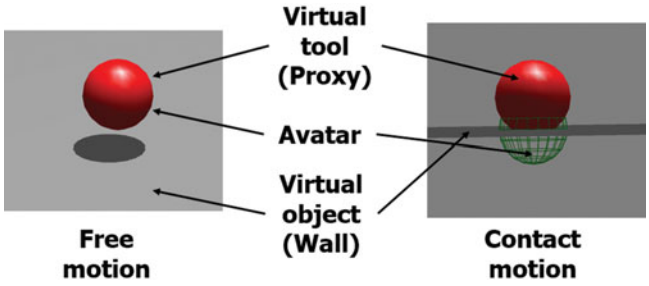


Fig. 13. Virtual wall simulation composed of an avatar, proxy, and virtual object (wall).

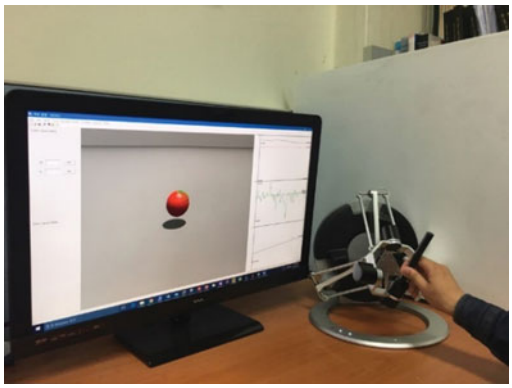


Fig. 14. Virtual wall simulation using Omega 6.0 haptic device.

Table III. Parameters of the haptic simulation.

Symbol	Quantity	value
m_d	Mass of the haptic device[5]	0.022 kg
b	Damping of the haptic device[5]	0.01 Ns/m
c_{vc}	Damping of the virtual coupling	0.006 Ns/m
m_e	Mass of the virtual tool	0.0001 kg
α_v	Velocity scaling factor	1
α_f	Force scaling factor	10

4. Experimental Verification

A one-DOF virtual wall simulation is carried out as shown in Fig. 13 to show the applicability of the proposed stability condition by comparing it with the previous stability conditions. The stability condition is examined in the z-direction. The commercial Omega 6.0 haptic device is used for the simulation as shown in Fig. 14.

The penalty method is used to generate the contact force between the virtual tool and wall. The stiffness of the penalty method should be higher than the stiffness of the virtual coupling to prevent the virtual tool from visually penetrating the object surface. The stiffness of the penalty method is set to three times the stiffness of the virtual coupling to see the effect of the contact stiffness that cannot be shown in the previous stability condition and for the transparency. The other parameters are set as given in Table III. The passivity condition and the absolute stability condition are compared with the proposed stability condition. The time step is changed in 0.002 s intervals from 0.002 s to 0.01 s. The maximum stiffness of the virtual coupling satisfying the passivity and absolute stability condition is acquired for each time step. The maximum stiffness satisfying the passivity condition is explicitly acquired from the passivity condition. The maximum gain satisfying the absolute stability condition is obtained at each time step. The stiffness changed at 0.5 N/m intervals is substituted into the absolute stability condition of the previous and the proposed.

Stability of the virtual wall simulation is experimentally tested by measuring the oscillations of the virtual tool. The position of the virtual tool is measured with a sampling frequency which is the

https://doi.org/10.1017/S0263574718001170 Published online by Cambridge University Press

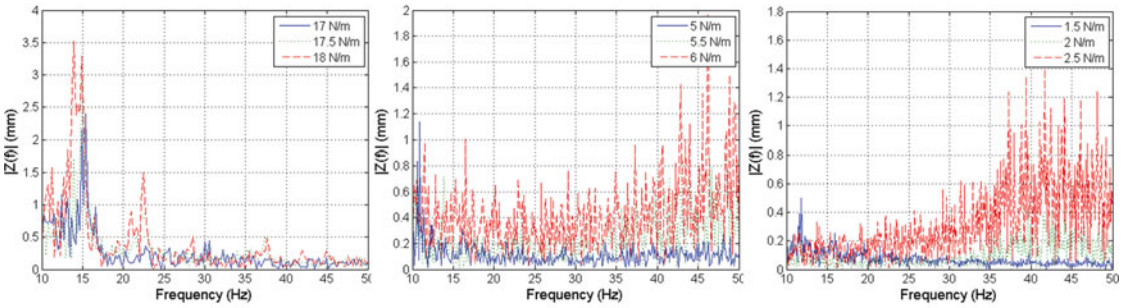


Fig. 15. Frequency spectrum of the virtual tool motion (Left: $\Delta T = 0.002$ s, Middle: $\Delta T = 0.004$ s, Right $\Delta T = 0.006$ s).

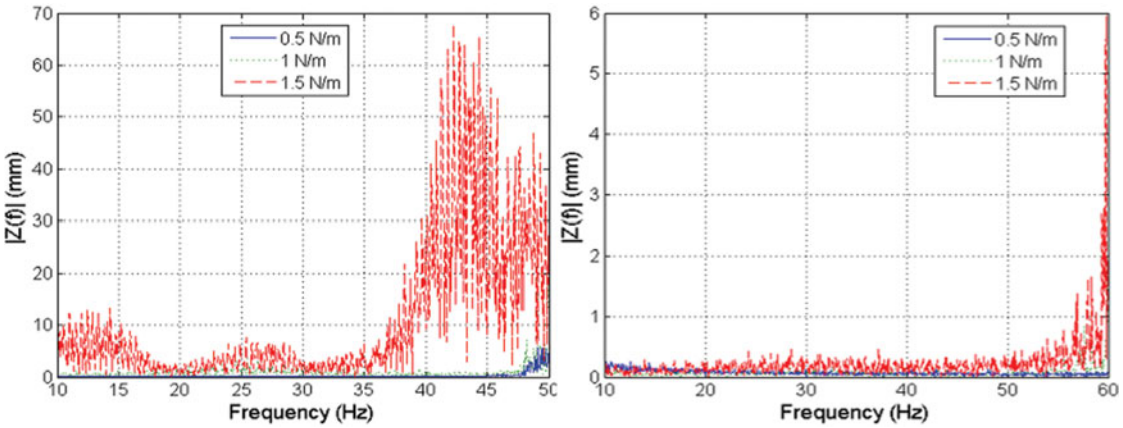


Fig. 16. Frequency spectrum of the virtual tool motion (Left: $\Delta T = 0.008$ s, Right $\Delta T = 0.010$ s).

Table IV. The maximum stiffness of conditions and experiment.

						Error	
Time step (s) Condition (N/m)	0.002	0.004	0.006	0.008	0.01	Mean	SD
Passivity	7	3.50	2.33	1.75	1.40	−2.00	4.92
Absolute stability (w/o V.E.)	7.29	3.64	2.42	1.81	1.45	−1.88	4.82
Proposed absolute stability (w/V.E.)	22.03	11	7.33	5.49	4.39	4.85	0.52
Experiment result	17.5	5.5	2.0	1.0	0	–	–

inverse of the time step because the oscillations of the virtual tool cause oscillation of the haptic device. More than 20 interactions with the virtual wall are conducted, changing the stiffness gain at 0.5 N/m intervals. The measured position data are analyzed in the frequency spectrum using a fast Fourier transform. Motion of the human operator is known to be generally limited under 20 Hz.[27] Maximum stiffness which does not cause oscillation exceeding 1 mm or more in frequency over 20 Hz is determined as the maximum stable stiffness. Figures 15 and 16 show the frequency spectrum of the virtual tool motion according to the time step size. The maximum stiffness satisfying the absolute stability condition of the previous and the proposed, the passivity condition, and the maximum stable stiffness determined experimentally are summarized in Table IV.

The experimental result shows that the maximum stiffness satisfying conditions and experimentally determined stiffness is low. The reason for the low stiffness is that the mass of the virtual tool is small and the semi-implicit integration becomes active as the time step increases. The stiffness of the penalty method set to three times the stiffness of the virtual coupling causes the stability problem at lower stiffness values. The experiment results show that the unstable behavior has different frequency spectra according to the time steps of the simulation. The absolute stability condition shows slightly

https://doi.org/10.1017/S0263574718001170 Published online by Cambridge University Press

higher stiffness than the passivity condition. Mean errors show that the passivity and absolute stability conditions are more conservative than the condition proposed in this paper. The standard deviation of the proposed condition is lower than the passivity and absolute stability conditions. This means that the proposed condition reflects more the tendency of the maximum stiffness gain over the time steps than the other conditions. The maximum stiffness of the passivity and absolute stability conditions is lower than the stable stiffness obtained in the experiment using the time steps of 0.002 s and 0.004 s. But it is higher in the time steps of 0.006 s, 0.008 s, and 0.01 s. The maximum stiffness of the proposed condition is higher than the experiment results with regular differences over time. The error seems to be caused by the modeling errors such as incorrect mass and damping of the haptic device. Behavior of the maximum stiffness with the proposed stability condition is more consistent with the experiment results.

5. Conclusion

This paper addresses the stability and the transparency of simulation involving rigid body dynamics of a virtual tool and interaction between the virtual tool and objects. Stability problem of the simulation has been traditionally considered as a stability problem of the haptic interface. The virtual environment has been usually assumed to be passive. Determination of the parameters of the virtual environment for the stability of the simulation has been thus left out. But the mass of the virtual tool, the maximum transmissible impedance of the virtual coupling and contacts are related to the stability and the transparency of the simulation. Absolute stability condition which has been often utilized does not include the components of the virtual environment. It hence tends to be more conservative and shows significant performance losses. Analysis of the stability and the transparency without considering the behavior of the virtual tool may be incorrect.

This paper extends the conventional two-port network analysis to include the virtual tool and the virtual interaction in the analysis of the stability and the performance. The traditional assumption that the human operator and the entire virtual environment are passive is alleviated to that the human operator and the virtual objects are passive. A velocity and force mapping matrix is employed to analyze the six-DOF haptic simulation. The proposed analysis shows the relation among the maximum transmissible impedance of the virtual coupling and the contact, the numerical-integration schemes, the mass of the virtual tool, and the absolute stability and the impedance transparency of the simulation.

The absolute stability condition obtained in this paper is experimentally verified using a one-DOF virtual wall simulation. The relation between the time steps and the maximum stable stiffness are acquired for the passivity, the absolute stability, and the proposed stability conditions. The proposed analysis can be utilized to determine the proper impedance of the virtual coupling, the virtual tool, the contact, and the numerical-integration schemes for given conditions such as the update rate of the simulation, the impedance of the haptic device, and the contact resolution method. An appropriate controller can be designed based on the proposed analysis of the stability and the transparency of the simulation involving the rigid dynamics of the virtual tool and interaction.

Acknowledgements

This work was supported by the National Research Foundation of Korea (NRF) grant funded by the Korean government (MEST) (No. NRF-2015R1A2A1A10054420), and Brain Korea 21 Plus program.

References

1. C. Basdogan, C. H. Ho and M. A. Srinivasan, "Virtual environments for medical training: Graphical and haptic simulation of laparoscopic common bile duct exploration," *IEEE/ASME Trans. Mechatron.* **6**, 269–285 (2001).
2. S. Y. Yi, H. S. Woo, W. J. Ahn, J. Y. Kwon and D. Y. Lee, "New colonoscopy simulator with improved haptic fidelity," *Adv. Robot.* **20**, 349–365 (2006).
3. K. Hashtrudi-Zaad, "Analysis of control architectures for teleoperation systems with impedance/admittance master and slave manipulators," *Int. J. Rob. Res.* **20**, 419–445 (2001).
4. J. E. Colgate and J. M. Brown, "Factors Affecting the Z-Width of a Haptic Display," *Proceedings of the 1994 IEEE International Conference on Robotics Automation* (1994) pp. 3205–3210. doi: 10.1109/ROBOT.1994.351077

https://doi.org/10.1017/S0263574718001170 Published online by Cambridge University Press

5. N. Diolaiti and G. Niemeyer, "Stability of haptic rendering: Discretization, quantization, time delay, and coulomb effects," *IEEE Trans. Robot.* **22**, 256–268 (2006).
6. R. J. Adams and B. Hannaford, "Stable haptic interaction with virtual environments," *IEEE Trans. Robot. Autom.* **15**, 465–474 (1999).
7. M. A. Otaduy and M. C. Lin, "A modular haptic rendering algorithm for stable and transparent 6-DOF manipulation," *IEEE Trans. Robot.* **22**, 751–762 (2006).
8. J. E. Colgate, M. C. Stanley and J. M. Brown, "Issues in the Haptic Display of Tool Use," *Proceedings of the 1995 IEEE/RSJ International Conference on Intelligent Robots and Systems. Human Robot Interaction and Cooperative Robots*, vol. **3**, IEEE Comput. Soc. Press (1995) pp. 140–145.
9. B. Hannaford and J. Ryu, "Time-domain passivity control of haptic interfaces," *IEEE Trans. Robot. Autom.* **18**, 1–10 (2002).
10. J. Ryu, C. Preusche, B. Hannaford and G. Hirzinger, "Time domain passivity control with reference energy following," *IEEE Trans. Control Syst. Technol.* **13**, 737–742 (2005).
11. K. Lee and D. Lee, "Adjusting output-limiter for stable haptic rendering in virtual environments," *IEEE Trans. Control Syst. Technol.* **17**, 768–779 (2009).
12. D. Lee and K. Huang, "Passive-set-position-modulation framework for interactive robotic systems," *IEEE Trans. Robot.* **26**, 354–369 (2010).
13. D. C. Ruspini, K. Kolarov and O. Khatib, "The Haptic Display of Complex Graphical Environments," *Proceedings of the 24th Annual Conference on Computer Graphics and Interactive Techniques SIGGRAPH1997*, ACM Press (1997) pp. 345–352. doi: 10.1145/258734.258878
14. C. B. Zilles and J. K. Salisbury, "A Constraint-Based GodObject Method for Haptic Display," *Proceedings of the 1995 IEEE/RSJ International Conference on Intelligent Robots and Systems. Human Robot InteractIon and Cooperative Robots*, vol. **3** (1995) pp. 146–151.
15. Adams, R. J. and Hannaford, B., "A Two-Port Framework for the Design of Unconditionally Stable Haptic Interfaces," *Proceedings of the 1998 IEEE/RSJ International Conference on Intelligent Robots and Systems. Innovations in Theory, PractIce and Applications (Cat. No.98CH36190)*, vol. **2** (1998) pp. 1254–1259.
16. J. E. Colgate and G. Schenkel, "Passivity of a Class of Sampled-Data Systems: Application to Haptic Interfaces," *Proceedings of the American Control Conference* (1994) pp. 3236–3240.
17. C. Duriez, F. Dubois, A. Kheddar and C. Andriot, "Realistic haptic rendering of interacting deformable objects in virtual environments," *Vis. Comput. Graph. IEEE Trans.* **12**, 36–47 (2006).
18. W. A. McNeely, K. D. Puterbaugh and J. J. Troy, "Six Degree-of-Freedom Haptic Rendering Using Voxel Sampling," *Proceedings of the 26th Annual Conference on Computer Graphics and Interactive Techniques SIGGRAPH1999* (1999) pp. 401–408. doi: 10.1145/311535.311600
19. W. A. Mcneely, K. D. Puterbaugh and J. J. Troy, "Voxel-Based 6-DOF Haptic Rendering Improvements," Haptics-e, **3**, (2006).
20. G. Cirio, M. Marchal, M. A. Otaduy and A. Lecuyer, "Six-Dof Haptic Interaction with Fluids, Solids, and Their Transitions," *Proceedings of the World Haptics Conference WHC2013* (2013) pp. 157–162. doi: 10.1109/WHC.2013.6548401
21. H. Xu and J. Barbic, "Adaptive 6-DoF haptic contact stiffness using the gauss map," *IEEE Trans. Haptics* **9**, 323–332 (2016).
22. F. Llewellyn, "Some fundamental properties of transmission systems," *Proceedings of the IRE*, vol. **2** (1952) pp. 271–283.
23. D. A. Lawrence, "Stability and transparency in bilateral teleoperation," *IEEE Trans. Robot. Autom.* **9**, 624–637 (1993).
24. A. M. Ousaid, D. S. Haliyo, S. Regnier and V. Hayward, "A stable and transparent microscale force feedback teleoperation system," *IEEE/ASME Trans. Mechatron.* **20**, 2593–2603 (2015).
25. D. J. Morris, E. F. Anderson and C. Peters, "A Modular Framework for Deformation and Fracture Using GPU Shaders," *Proceedings of the 18th International Conference on Virtual Systems & Multimedia* (2012) pp. 267–274. doi: 10.1109/VSMM.2012.6365934
26. S. Hasegawa and M. Sato, "Real-time rigid body simulation for haptic interactions based on contact volume of polygonal objects," *Comput. Graph. Forum* **23**, 529–538 (2004).
27. D. Ryu, J. Song, S. Kang and M. Kim, "Frequency domain stability observer and active damping control for stable haptic interaction," *IET Control Theory Appl.* **2**, 261–268 (2008).

https://doi.org/10.1017/S0263574718001170 Published online by Cambridge University Press